

Article

Computational Fluid Dynamics Investigation of the Spacing of the Aerodynamic Characteristics for Multiple Wingsails on Ships

Hongming Wang ^{1,2}, Chen Li ^{1,2,*}, Caibao Zuo ¹, Junfu Yuan ^{1,2} and Binxin Wu ^{1,3}

¹ Marine and Electrical Engineering College, Jiangsu Maritime Institute, Nanjing 211170, China; 20060178@jmi.edu.cn (H.W.); 20178005@jmi.edu.cn (C.Z.); 20070904@jmi.edu.cn (J.Y.); bwu66@zju.edu.cn (B.W.)

² Jiangsu Ship Energy-Saving Engineering Technology Center, Nanjing 211170, China

³ College of Biosystems Engineering and Food Science, Zhejiang University, Hangzhou 310058, China

* Correspondence: 20158112@jmi.edu.cn

Abstract: Wind energy, as an inexhaustible energy source, has become a focal point in the development of new energy for ships. Sail-assisted technology, which leverages wind power, has been successfully applied to ship propulsion. The propulsion performance of sail-assisted ships is affected by the interference characteristics among multiple wingsails. To investigate interference characteristics, an arrangement scheme involving two-element wingsails and considering the relative wind direction angle was established. To obtain the inter-stage interference characteristics of wingsails, the Reynolds average N-S equation was used in the numerical simulation conducted under steady operating conditions. The results indicate that, at the relative wind angles of 30°, 90°, and 120°, the minimum horizontal spacing in a single row arrangement scheme is 1.5c. However, at relative wind angles of 90° and 120°, inter-stage interference may induce stall conditions in the wingsails. In a double-row arrangement scheme, the wake of the upstream wingsail interferes with the flow of the downstream sail at relative wind angles of 90°. An optimal propulsion performance is achieved with a horizontal spacing of 4c and a longitudinal spacing of 10c. Moreover, the interference performance of the two-element wingsails can be enhanced through a horizontal offset arrangement. This study provides a reference for the arrangement of wingsails on ships.



Citation: Wang, H.; Li, C.; Zuo, C.; Yuan, J.; Wu, B. Computational Fluid Dynamics Investigation of the Spacing of the Aerodynamic Characteristics for Multiple Wingsails on Ships. *J. Mar. Sci. Eng.* **2024**, *12*, 985. <https://doi.org/10.3390/jmse12060985>

Academic Editor: Md Jahir Rizvi

Received: 15 April 2024

Revised: 5 June 2024

Accepted: 7 June 2024

Published: 12 June 2024



Copyright: © 2024 by the authors. Licensee MDPI, Basel, Switzerland. This article is an open access article distributed under the terms and conditions of the Creative Commons Attribution (CC BY) license (<https://creativecommons.org/licenses/by/4.0/>).

1. Introduction

The International Maritime Organization (IMO) has adopted increasingly strict greenhouse gas emission regulations [1]. In the “Preliminary Strategy for Reducing Greenhouse Gas Emissions from Ships”, adopted by the 72nd session of the Maritime Environmental Protection Committee in 2018, it was explicitly stated that by 2030, the average carbon emission intensity per transport unit in the global shipping industry should be reduced by at least 40% compared to 2008. Efforts will be made to reduce it by 70% by 2050 [2]. Hence, reducing carbon emissions through technological or operational means is considered to be the primary method for existing ships to meet the IMO’s carbon reduction goals. Encouraging the development of alternative low-carbon/zero-carbon fuels or techniques has also become a consensus among countries [3].

Sail-assisted technology, which harnesses wind energy, represents a significant development in ship propulsion, addressing the maritime industry’s pursuit of new energy solutions. To enhance the propulsion performance of sail-assisted ships by fully utilizing the deck space, multiple sails are usually arranged on the ship’s deck [4].

Due to the excellent aerodynamic characteristics of wingsails, their application in small vessels such as unmanned boats has seen rapid development, with the emergence of “Stars and Stripes” catamarans [5], “Atlantis” catamarans [6], X1 catamarans [7], WASP ASV prototype ships [8], “A-Tirma G2” prototype ships [9], “Submaran S10” unmanned

boats [10], “Saildrone” USV [11], and “Datamaran” catamarans [12]. Among them, two sets of wingsails were installed on the “A-Tirma G2” prototype ship. The unmanned submarine is 2 m long, with a wingsail height of 1.05 m, and the wing profile adopts NACA0009. Domínguez-Brito [13] evaluated the interference effect between these two sets of wingsails when designing and analyzed the performance impact while varying the spacing between them through experiments. The results show that appropriate spacing can increase the propulsion force.

Thus far, many scholars have investigated the multi-sail interference characteristics of sail-assisted vessels. Fujiwara et al. [14,15] evaluated the impact of sail–sail interactions on the aerodynamic performance of sails through CFD simulations. According to their results, the interference effect between the sails reduces thrust propulsion by more than 7%. Jo [16] optimized the wingsail model to analyze the aerodynamic characteristics of multiple wingsails through CFD numerical simulation. Compared with the initial multi-row wingsail model, the average thrust performance of the optimized wingsails was improved in all wind directions, with an overall improvement in the thrust performance of 9–11%. Drawing on the design experience of Jo, the angle of attack and flap deflection of wingsails were optimized to achieve enhanced lift. Qiao [17] conducted numerical simulations and experimental verification on the propulsion performance of a variable-angle sail with a modified main wing. The results indicate that the thrust coefficient increased with the increase in the spacing between the sails. If the spacing was too small, it would increase aerodynamic interaction. Under the wake interference of the upstream sail, the downstream sail begins to stall. Zhang [18] took the 76,000 DWT Panama bulk carrier hull and selected the NACA0016 airfoil as the sail and analyzed the effects of sail spacing, wind direction, and rotation angles on the propulsion performance of the modeled ship. The sail had an excellent energy-saving effect, with a maximum EEDI reduction rate of 13%.

Although the application of wingsail-assisted navigation technology in commercial ships has developed rapidly in recent years, some commercial ships, especially VLCC decks, have not been fully utilized in sail-assisted navigation design due to the large deck area of commercial ships. However, the unreasonable arrangement of multiple sails can cause interference effects between the wingsails, and there is currently limited research on this topic. This paper uses numerical methods to simulate the aerodynamic interference effects of two-element wingsails and obtains the aerodynamic influence law of different wind directions on the sail arrangement. It provides a theoretical reference for multi-sail arrangement.

This study is structured in four sections. Section 1 introduces the background, history, and application of sail-assisted navigation technology, with a focus on multisail interference research. Section 2 introduces the physical model of the wingsail and the multisail arrangement scheme, using numerical simulation methods including computational domain, grids, a reliability verification of the mesh, and an experimental verification of numerical methods to ensure the reliability of the numerical calculation results. Section 3 is the analysis and discussion of numerical simulation results, focusing on the interference characteristics of multiple sails at relative wind angles of 30°, 90°, and 120°, obtaining the optimal layout scheme of multiple sails. Section 4 is the conclusion and summary, which summarize the research contributions of this paper and provide directions for future research.

2. Physical Models and Numerical Methods

2.1. Two-Element Wingsail Airfoil Model and Layout Plan

The two-element wingsail airfoil refers to the contour characteristics of the wingsail section, which is similar to a wing airfoil equipped with flaps, as shown in Figure 1 [4]. The front and flap airfoils are selected from the NACA 4-digit series airfoils with different maximum thicknesses. The object of this study is a two-element wingsail composed of the main wing and a flap, built upon Daniel’s prior research [19]. The geometric cross-section of the two-element wingsail is illustrated in Figure 2, with the NACA0018 airfoil for the main wing and the NACA0015 airfoil for the flap. Table 1 shows the design parameters

of the wingsail, including the total chord length (c), flap chord length ratio (c_2/c), flap deflection angle of the two-element wingsail airfoil (δ), the position of the flap rotation (X_r), and the relative width of the gap (g).



Figure 1. Oceanwings designed by AYRO.

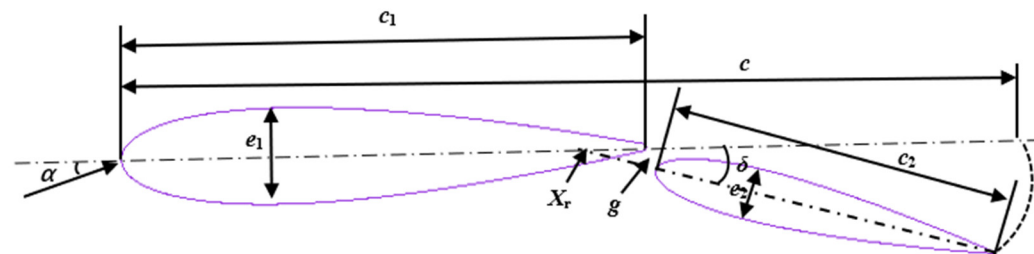


Figure 2. Cross-section of two-element wingsail airfoil model.

Table 1. Design parameters of the wingsail.

Parameter	Symbol	Value Range
Total chord of the wingsail	c	3.5 m
c_2/c	0.4	
Reynolds number	Re	2.4×10^6
Flap deflection angle	δ	$0\text{--}25^\circ$
Angle of attack of the wingsail (AOA)	α	$0\text{--}20^\circ$
Non-dimensional slot width	g	2.4%
Flap rotation axis position	X_r	90%

To analyze the influence of the flow field between adjacent wingsails, multiple wingsails were arranged, as shown in Figure 3. The distance between adjacent wingsails along the ship's width is defined as the horizontal spacing, while the distance between adjacent two-element wingsails parallel to the ship's hull is defined as the longitudinal spacing. These spacings are expressed as multiples of the total chord length (c) of the two-element wingsail. By adjusting the horizontal and longitudinal spacings, the ship can achieve stable and efficient sail propulsion. The two-element wingsails closest to the deck superstructure in the stern of the ship are designated as Wingsail 1, followed by Wingsail 2 and Wingsail 3, as illustrated in Figure 4. Using a layout strategy of the two-element wingsails on the ship at various wind angles [20], and considering the structural characteristics of the two-element wingsail, we propose a configuration scheme for the initial attack angle and flap deflection angle of the two-element wingsails at different relative wind angles. This scheme is detailed in Table 2.



Figure 3. “A-Tirma G2” prototype ships.

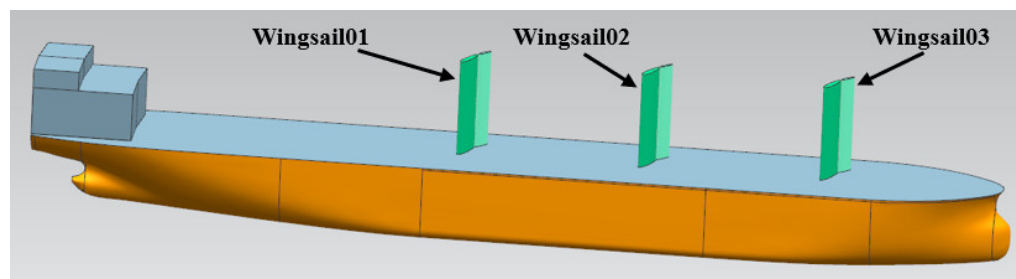


Figure 4. Layout of single-row two-element wingsails spaced along the centerline of the ship.

Table 2. Configuration scheme for initial angle of attack and flap deflection angle of wingsails.

Relative Wind Direction Angle	Wingsail Parameters	Wingsail 1	Wingsail 2	Wingsail 3
30 ($^{\circ}$)	δ ($^{\circ}$)	5	5	5
	α ($^{\circ}$)	8	8	8
90 ($^{\circ}$)	δ ($^{\circ}$)	25	25	25
	α ($^{\circ}$)	12	12	12
120 ($^{\circ}$)	δ ($^{\circ}$)	15	15	15
	α ($^{\circ}$)	10	10	10

When investigating the interference characteristics of two-element wingsails, we sequentially analyzed the longitudinal spacing schemes for relative wind angles of 30° , 90° , and 120° , as presented in Table 3, to examine how varying spacings affect the interference characteristics of the two-element wingsails.

Table 3. Layout scheme of two-element wingsails on ship.

Types	Case 1	Case 2	Case 3
Longitudinal spacing	$1c$	$1.5c$	$2c$

2.2. Computational Domain and Grid

ANSYS Fluent software, version 18.2 (Ansys Fluent, Canonsburg, PA, USA) was adopted for the numerical simulation of the two-element wingsail 2D model. Although

the two-dimensional model cannot display the details of corner separation, it simplifies the physical model, reduces the total amount of mesh, and has great benefits for numerical simulation. Based on the structural characteristics of the two-element wingsail airfoil depicted in Figure 2, a two-dimensional numerical calculation domain was established, as illustrated in Figure 5a. To minimize the impact of computational domain boundaries on the external flow field of the airfoil, lengths of $12c$ in front of the airfoil and $20c$ behind the airfoil, as well as a width of $12c$, were selected. The computational domain is rectangular ($32c \times 24c$). The inlet boundary and left and right boundaries of the computational domain are configured as velocity inlets, with an incoming turbulence intensity of 1% and a turbulence viscosity ratio of 7 [21]. Given the selection of the Transition SST model [22,23] for turbulence simulation, the intermittency factor in the fully turbulent state was set as 1. The outlet boundary was configured as the pressure outlet, with a set total pressure of 101,325 Pa. The airfoil wall was assigned a non-slip wall condition.

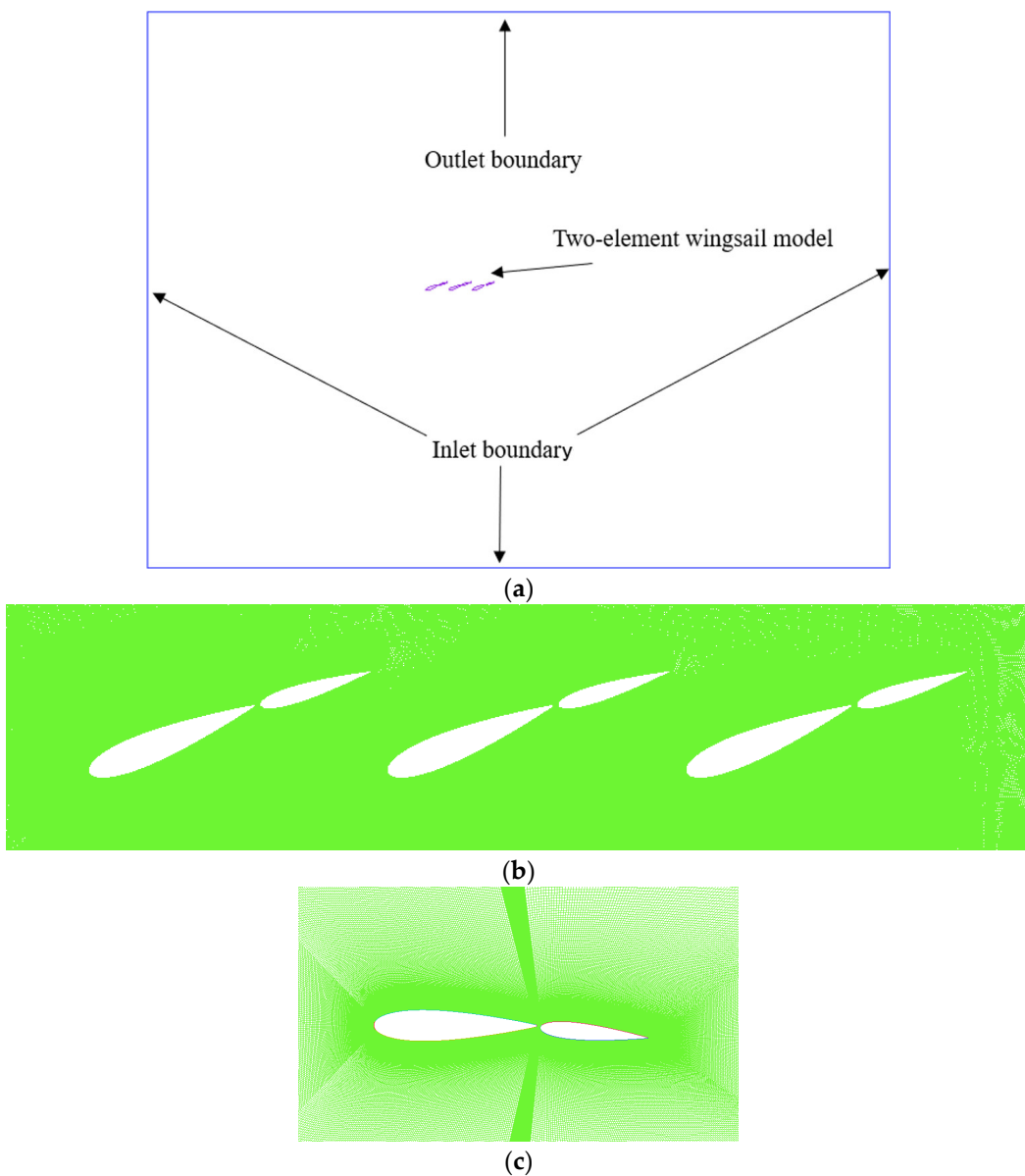


Figure 5. Cont.

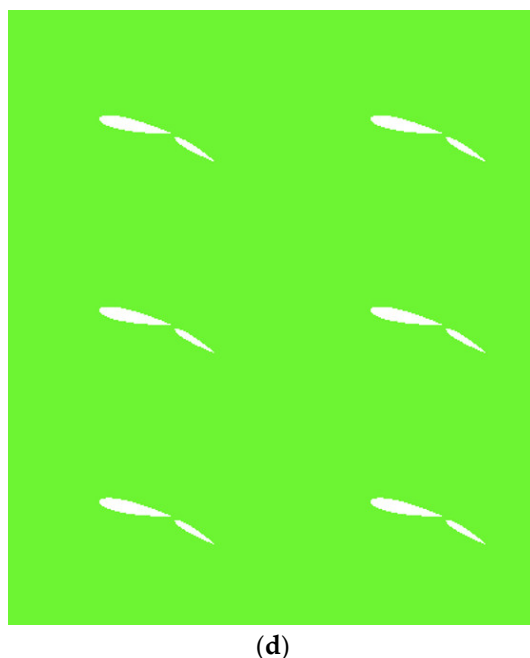


Figure 5. Computational domain and grid of two-element wingsail airfoil. (a) Computational domain and the (b) 2D grid of the single-row arrangement scheme. (c) The grid in the gap region and the (d) 2D grid of the double-row arrangement scheme.

For the convenience of calculation, the domain of the double-row arrangement scheme is consistent with that of the single-row layout scheme.

In CFD calculations, grid quality is crucial for determining the accuracy and computational efficiency of numerical calculations. For this study, an unstructured grid in ANSYS ICEM was used to mesh the two-dimensional model within the computational domain, involving triangular meshes, prism layer meshes, and mesh surface reconstruction models, as illustrated in Figure 5b. In order to control the total amount of grid, the computational domain was divided into zones, with the middle part being a rectangular wingsail with a length of $3c$ and a width of $1.5c$; the grid size used in the far field is larger. The grid in the gap region was refined and encrypted as Figure 5c. The mesh size on the surface of the wingsail is $0.4\%c$. The non-dimensional wall distance, y^+ , was maintained at less than or equal to 1 to fulfill the requirements of turbulence models for boundary layer simulation [24,25]. The height of the first grid layer on the wingsail surface was set as $0.85 \times 10^{-5}c$, with a boundary layer growth rate specified as 1.05, the number of boundary layers as 20, and the total number of grids as approximately 1.24×10^6 . The grid size of the double-row arrangement scheme is consistent with that of the single-row arrangement scheme, and the grid model is shown in Figure 5d; the total number of grids is approximately 2.54×10^6 .

2.3. Grid Independence Analysis

To ensure that the number of grids did not affect the aerodynamic characteristics of the two-element wingsail airfoil, the Transition SST turbulence model was used to estimate four different grid numbers (6.3×10^5 , 9.5×10^5 , 1.24×10^6 , and 1.54×10^6) for simulation accuracy. The surface grids of these four grid sizes of wing sails are shown in Table 4. The minimum grid size on the surface of the wingsail was set to $0.03\%c$.

Figure 6 shows the lift coefficient C_L and drag coefficient C_D of the Wingsail 1 airfoil for the Case 3 scheme with a flap deflection angle of 0° at $Re = 2.4 \times 10^6$. In Figure 6, it is evident that the drag coefficient remains basically unchanged with an increase in grid number, while the lift coefficient fluctuates slightly with increased grid number. However, the fluctuation range stays within 0.5%, aligning with the numerical calculation requirements. Since the meshing strategy of the double-row arrangement scheme is the same as that of the

single-row arrangement scheme, it can also be considered that the grid of the double-row arrangement scheme meets the requirements.

Table 4. Setting of wingsail surface grid parameters.

Mesh Type	Mesh Size of Wingsail Surface	Total Grid Numbers
Rough mesh	1.2% c	6.3×10^5
Medium mesh	0.8% c	9.5×10^5
Fine mesh	0.4% c	1.24×10^6
Finest mesh	0.25% c	1.54×10^6

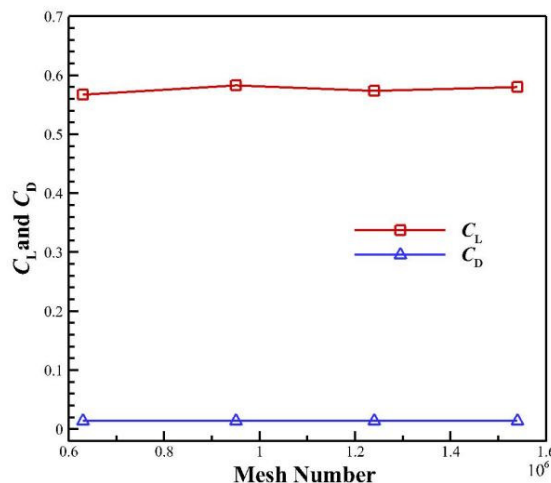


Figure 6. Sensitivity of grid vs. lift coefficient C_L and drag coefficient C_D at $\alpha = 6^\circ$.

To further verify the reliability of the grid, Figure 7 illustrates the effect of grid size on boundary layer transition using the Transition SST turbulence model at $Re = 2.4 \times 10^6$.

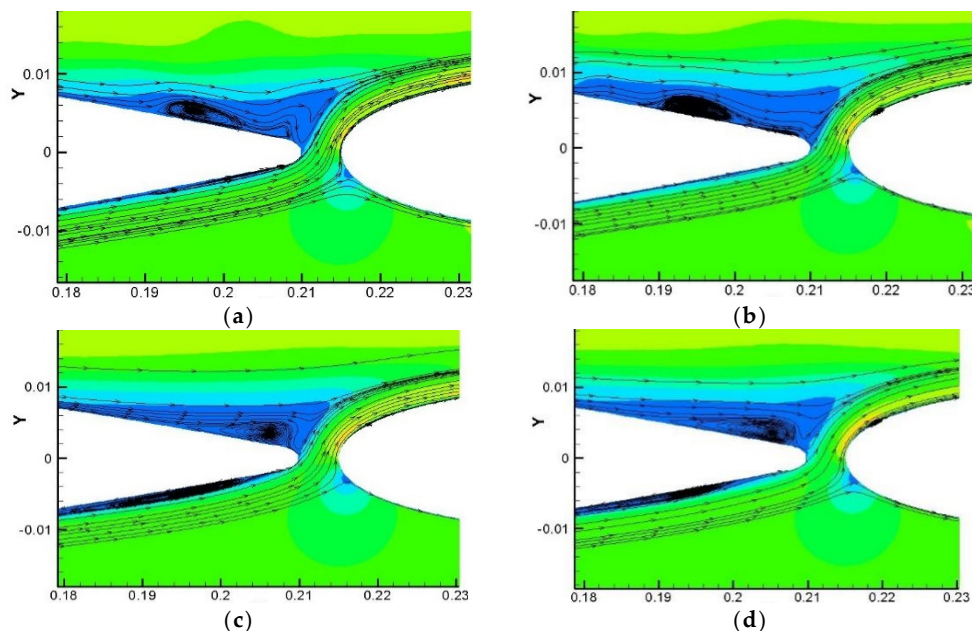


Figure 7. Laminar separation bubbles with different grid numbers at $\alpha = 6^\circ$. Grid sizes of (a) 6.3×10^5 , (b) 9.5×10^5 , (c) 1.24×10^6 , and (d) 1.54×10^6 .

In Figure 7, it can be seen that there is a significant laminar separation bubble on the main wing pressure surface, the size of which is basically consistent in the grid of 1.24×10^6

and 1.54×10^6 , while there is no obvious laminar separation bubble in the grid of 6.3×10^5 and 9.5×10^5 . Considering the increase in calculation cost caused by a larger grid number, the grid number used in the calculation domain of the two-dimensional model was 1.24×10^6 .

2.4. Reliability Analysis of Numerical Methods

Before simulating a two-element wingsail airfoil, it is necessary to conduct a fundamental validation of the numerical simulation method. Experimental data from the NACA0018 airfoil in the Wind Tunnel Laboratory of Delft University [26] were employed to verify the accuracy of the Transition SST turbulence model, which was used to predict the performance and capture flow field information in this paper. To ensure the accuracy of the numerical simulation method, the grid type requires the same type of grid as the two-element wingsail airfoil model.

The lift–drag characteristics of the NACA0018 airfoil were compared using experimental data [27–30] and numerical results at $Re = 1.6 \times 10^5$, as illustrated in Figure 8. The lift–drag coefficient, calculated using the Transition SST turbulence model, shows good agreement with experimental data. When the angle of attack is large, the experimental lift coefficient is slightly less than the numerical result, and the drag coefficient also exhibits fluctuations; the difference ratio between experimental data and numerical simulation data is less than 8%. This is because the airfoil boundary layer plays a crucial role in airflow separation during the transition process as the angle of attack increases. The Transition SST turbulence model can also capture the boundary layer transition process due to two additional variable transport equations. These calculation results also closely align with experimental values, demonstrating that the numerical simulation method used in this paper is relatively accurate in predicting the aerodynamic performance of airfoils.

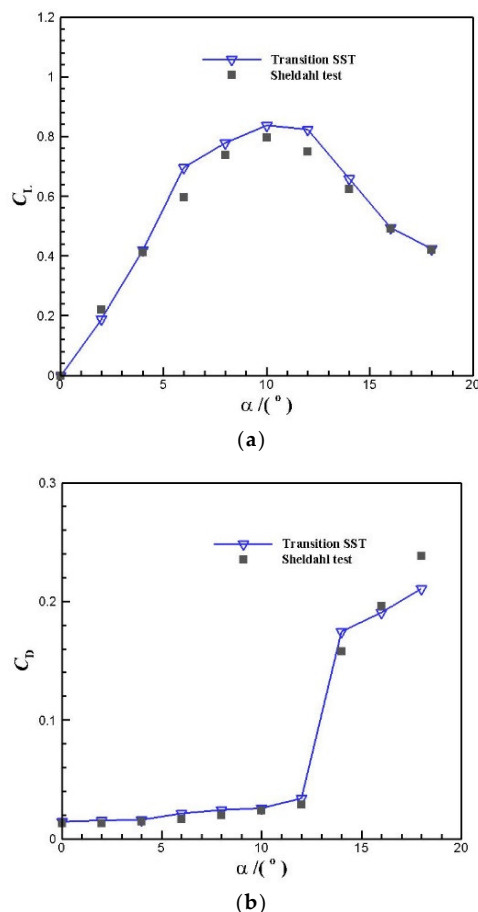


Figure 8. Comparative analysis of experimental results [28] and numerical simulation results: (a) C_L vs. α . (b) C_D vs. α .

As the model has verified, parameter study is important for enhancing the model, and it can be used to predict results that are difficult to obtain via experiments.

3. Results and Discussion

The lift–drag coefficient and propulsion coefficient are important dimensionless parameters for measuring the propulsion performance of wingsails. An analysis was performed on the model to intuitively understand the lift–drag coefficient and propulsion coefficient, as shown in Figure 9.

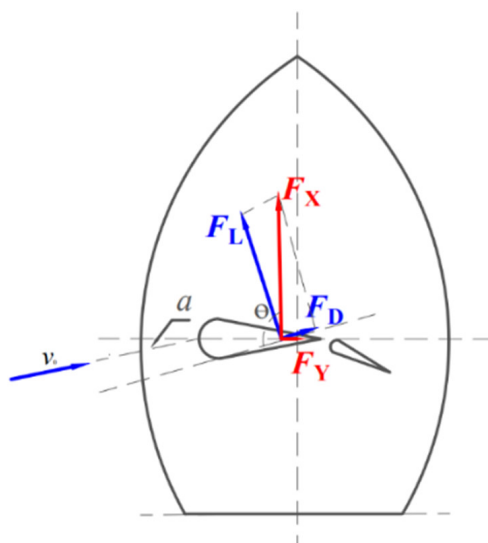


Figure 9. A force analysis of a wingsail on a ship with wind at 100 degrees.

The positive direction of the x-axis is toward the bow along the length of the ship, and the positive direction of the y-axis is toward starboard along the width of the ship. The angle between the incoming wind direction and the bow is defined as the relative wind direction angle θ . The relative wind direction toward the bow is 0° and this increases counterclockwise when looking down at the ship, while the relative wind direction from the stern is 180° . The lift F_L and resistance F_D of the wingsail are combined and recomposed to obtain the auxiliary forward thrust F_X along the ship's heading and the side thrust F_Y perpendicular to the ship's heading.

The lift coefficient C_L and drag coefficient C_D of the two-element wingsail airfoil are expressed as follows [31]:

$$C_L = \frac{F_L}{0.5\rho v_0^2 c} \quad (1)$$

$$C_D = \frac{F_D}{0.5\rho v_0^2 c} \quad (2)$$

where c is the total chord length of the two-element wingsail airfoil, v_0 is the velocity of inflow, ρ is the density of the air, F_L is the lift force, and F_D is the drag force. The auxiliary forward thrust coefficient C_X and side thrust coefficient C_Y of the ship's wingsail are expressed as follows:

$$C_X = C_L \sin \theta - C_D \cos \theta \quad (3)$$

$$C_Y = C_L \cos \theta + C_D \sin \theta \quad (4)$$

3.1. Interference Characteristics at a Relative Wind Direction Angle of 30°

Table 5 lists the propulsion performance of each group of two-element wingsails with different horizontal spacings at $Re = 2.4 \times 10^6$. And the pressure cloud picture of multiple sets of two-element wingsails at $\theta = 30^\circ$ is shown in Figure 10. Table 4 shows that, compared

to Case 1, the overall performances of Case 2 and Case 3 are relatively close, with the lift coefficient increasing by 4.1% and auxiliary thrust coefficient increasing by 4.9%. And the side thrust coefficient also increased, but the average value was still less than 1.1, meeting the design requirements. Among the three types of two-element wingsail arrangement schemes, Wingsail 1 features the highest lift coefficient and negative drag coefficient, while Wingsail 3 features the lowest lift coefficient, which is influenced by the interference of the flow field from the upwind wingsails, as shown in Figure 10.

Table 5. Propulsion performance of the wingsail at different transverse distances at $\theta = 30^\circ$.

Horizontal Spacing Type	Wingsail Type	C_L	C_D	C_X	C_Y
Case 1	Wingsail 1	2.085	-0.091	1.122	1.761
	Wingsail 2	0.872	0.120	0.332	0.815
	Wingsail 3	0.398	0.076	0.134	0.383
	Average value	1.120	0.035	0.529	0.986
Case 2	Wingsail 1	1.839	-0.057	0.969	1.565
	Wingsail 2	1.039	0.082	0.449	0.941
	Wingsail 3	0.618	0.079	0.241	0.575
	Average value	1.166	0.035	0.555	1.027
Case 3	Wingsail 1	1.644	-0.034	0.851	1.407
	Wingsail 2	1.097	0.059	0.497	0.981
	Wingsail 3	0.754	0.073	0.313	0.689
	Average value	1.165	0.033	0.553	1.025

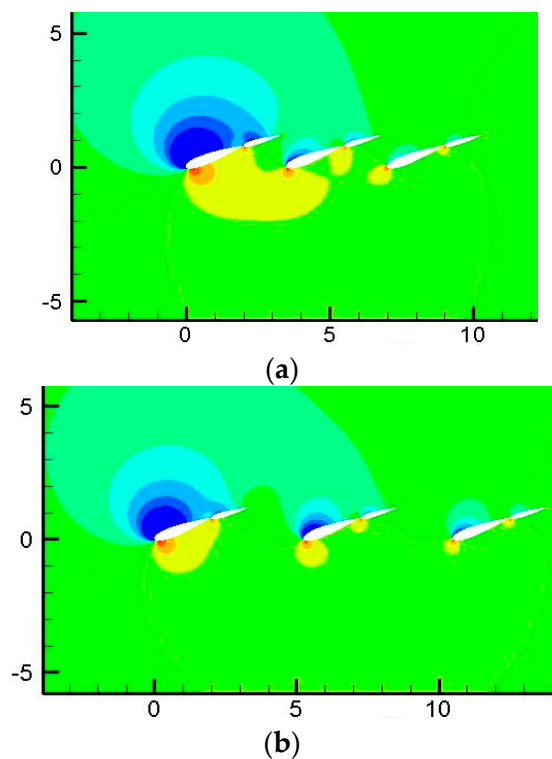


Figure 10. Cont.

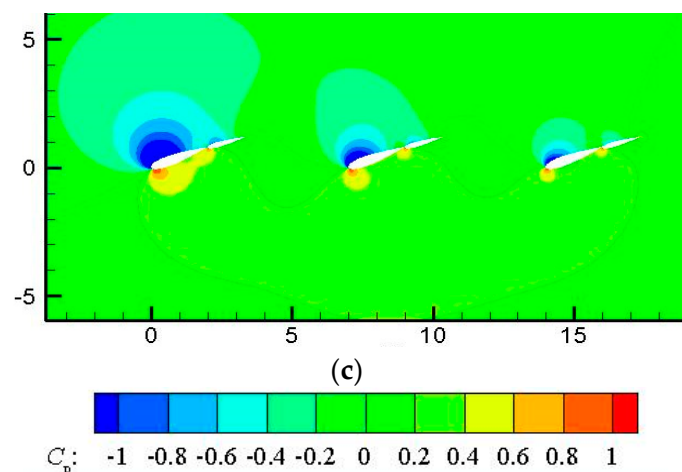


Figure 10. Static pressure cloud of two-element wingsail with horizontal wind at $\theta = 30^\circ$. (a) Case 1. (b) Case 2. (c) Case 3.

In Figure 10a, it can be observed that Wingsail 1 has the highest negative pressure, Wingsail 3 has almost no negative pressure, and positive pressure is not separated between the three sets of two-element wingsails in Case 1. Due to the close horizontal spacing of the two-element wingsails, the positive pressure of the upstream wingsail interferes with the negative pressure on the suction surface of the downstream wingsail, reducing the lift of the downstream wingsail. In Figure 10b,c, it can be seen that, as the horizontal spacing increases, the negative pressure of Wingsail 1 decreases, while the negative pressure of Wingsail 2 and Wingsail 3 increases. This is consistent with the lift coefficients in Table 4. The pressure between the trailing edge of Wingsail 1 and the leading edge of Wingsail 2 approaches 0, indicating that the interference effect of the upstream wingsail on the negative pressure of the downstream wingsail suction surface is weakened. There is almost no such inter-stage interference effect shown in Figure 10c.

Figure 11 shows the velocity cloud map of the wingsails at a wind direction angle of 30° . In Figure 11a, Wingsail 1 has an interference effect on the incoming flow velocity of Wingsail 2. The incoming flow velocity at the leading edge of Wingsail 2 is significantly reduced, therefore reducing the lift coefficient of Wingsail 2. However, this phenomenon does not exist in Figure 11b,c. In Figure 12, the propulsion performance of each group of wingsails when the Reynolds number increases to 4.4×10^6 is shown. It can be observed that the average auxiliary thrust coefficient of Case 2 was highest, with an increase of 4.5% in the average lift coefficient and 9.7% in the average auxiliary thrust coefficient compared to Case 1 at $Re = 4.4 \times 10^6$. The average side thrust coefficient met the design requirements as well.

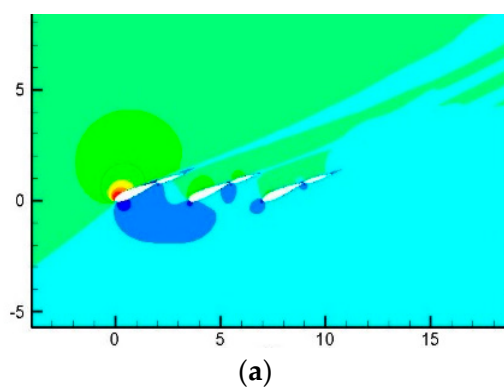


Figure 11. Cont.

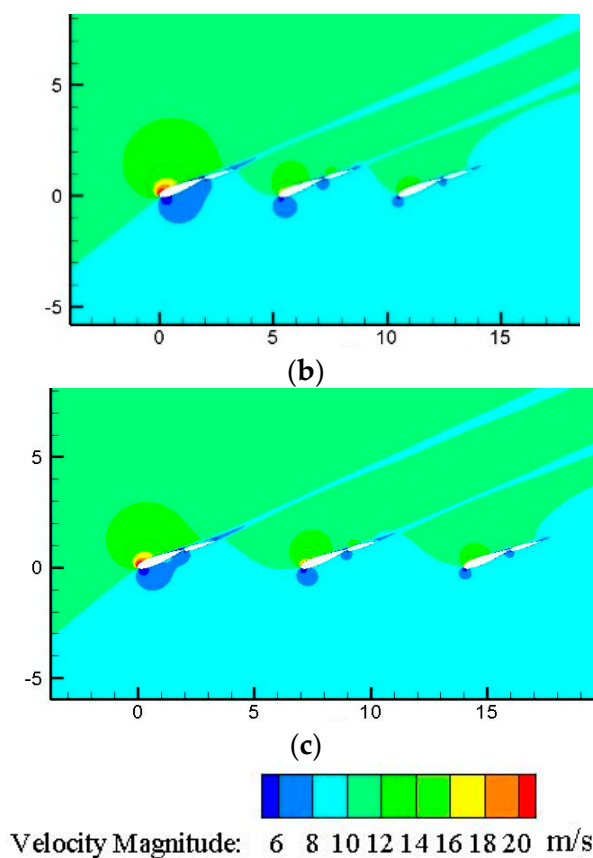


Figure 11. Velocity fields of two-element wingsails with horizontal wind at $\theta = 30^\circ$. (a) Case 1. (b) Case 2. (c) Case 3.

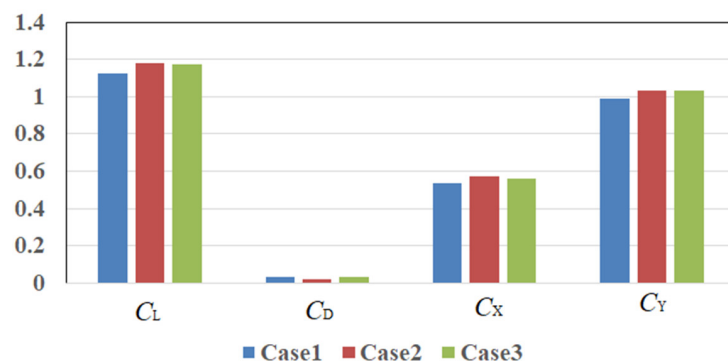


Figure 12. Performance of the wingsail at different spacings at $Re = 4.4 \times 10^6$.

3.2. Interference Characteristics at a Relative Wind Direction Angle of 90°

Figure 13 shows a performance comparison of each set of wingsails with different horizontal spacings at a wind direction angle of 90° . It can be seen that the auxiliary thrust coefficient of Case 2 is the highest, reaching 1.85, while the average side thrust coefficient is only 0.223, which fulfills the design requirements. This is consistent with the selection scheme of horizontal spacing when the relative wind direction angle is 30° . By comparing their drag coefficients and Figure 14, it is evident that flow separation exists on the flap suction surface of Case 1, Case 2, and Case 3 due to the interference effect between the wingsail stages, leading to wingsail stall. However, there is no flow separation phenomenon in a single group of two-element wingsails (as shown in Figure 14a) at the same attack angle and flap deflection angle.

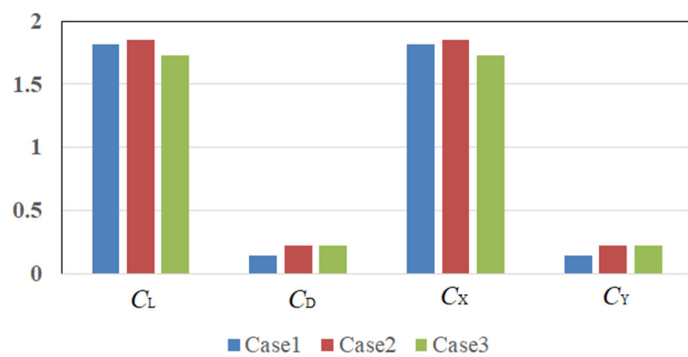


Figure 13. Performance comparison of the wingsails at different horizontal spacings with the wind at $\theta = 90^\circ$.

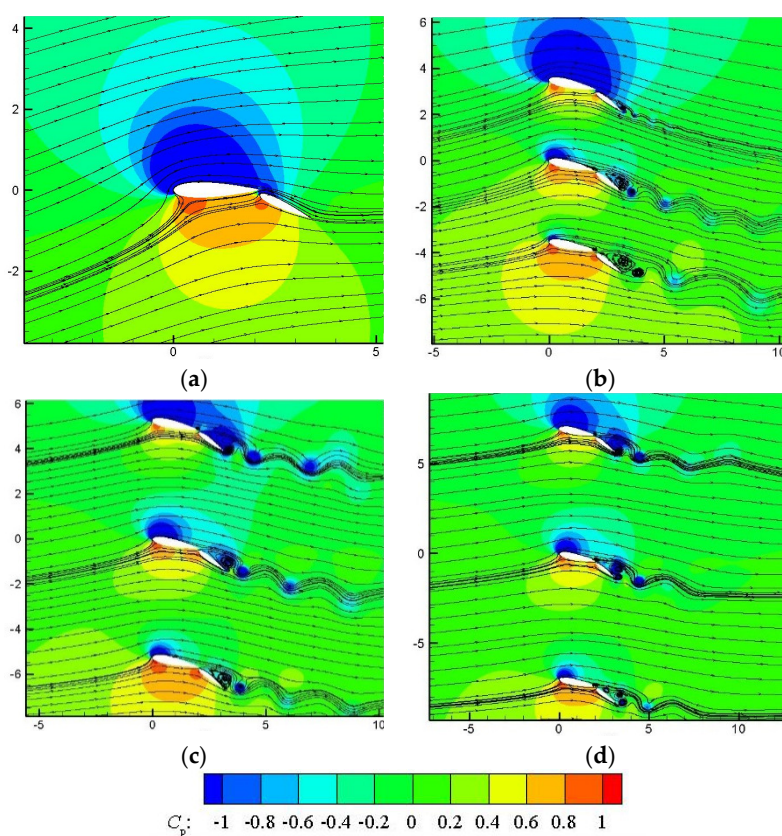


Figure 14. Pressure distribution and streamlines of wingsails at $\theta = 90^\circ$. (a) Single two-element wing-sail. (b) Case 1. (c) Case 2. (d) Case 3.

3.3. Interference Characteristics at a Wind Direction Angle of 120°

Figure 15 shows a performance comparison of each group of two-element wingsails with different horizontal spacings at a wind direction angle of 120° . Notably, Case 2 exhibits the highest auxiliary thrust coefficient, while the average side thrust coefficient is only 0.832, directed towards the port side of the ship. Importantly, the wingsail flow remained unseparated, as illustrated in Figure 16, adhering to the design requirements. This observation is consistent with the selected horizontal spacing when the wind direction angle is 30° and 90° . The auxiliary thrust coefficient for Case 2 may be further improved by adjusting the angle of attack.

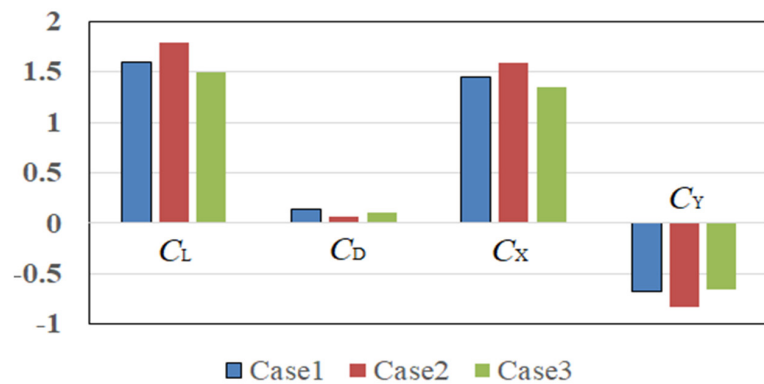


Figure 15. Performance comparison of single row wingsails at different lateral spacings at $\theta = 120^\circ$.

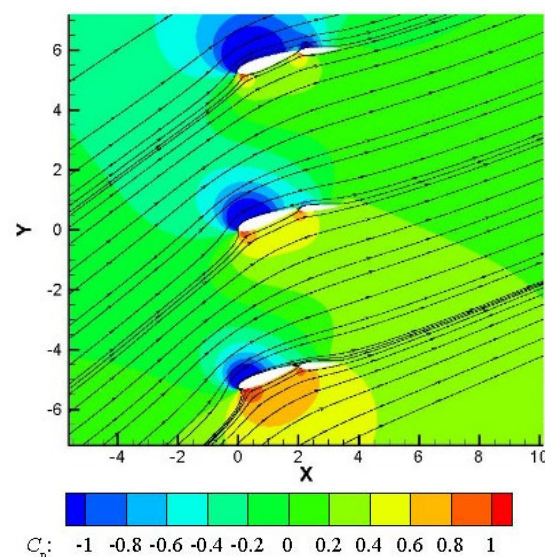


Figure 16. Streamline distribution of Case 2 at $\theta = 120^\circ$.

3.4. Interference Characteristics of Double-Row Wingsails at a Relative Wind Direction Angle of 90°

According to the scheme of single-row wingsail arrangement, the double-row arrangement of wingsails on the ship deck was implemented, as shown in Figure 17. The arrangement scheme is detailed in Table 6. A numerical simulation of the interference characteristics of the double-row wingsails was carried out and Figure 18 shows the velocity cloud map of each group of wingsails with different longitudinal spacings and a horizontal spacing of $1.5c$ at $Re = 2.4 \times 10^6$.

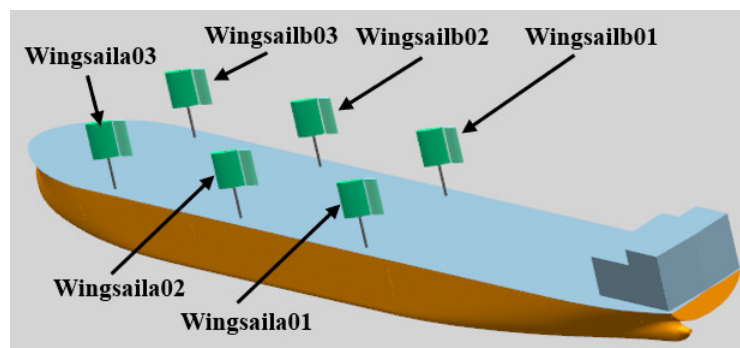
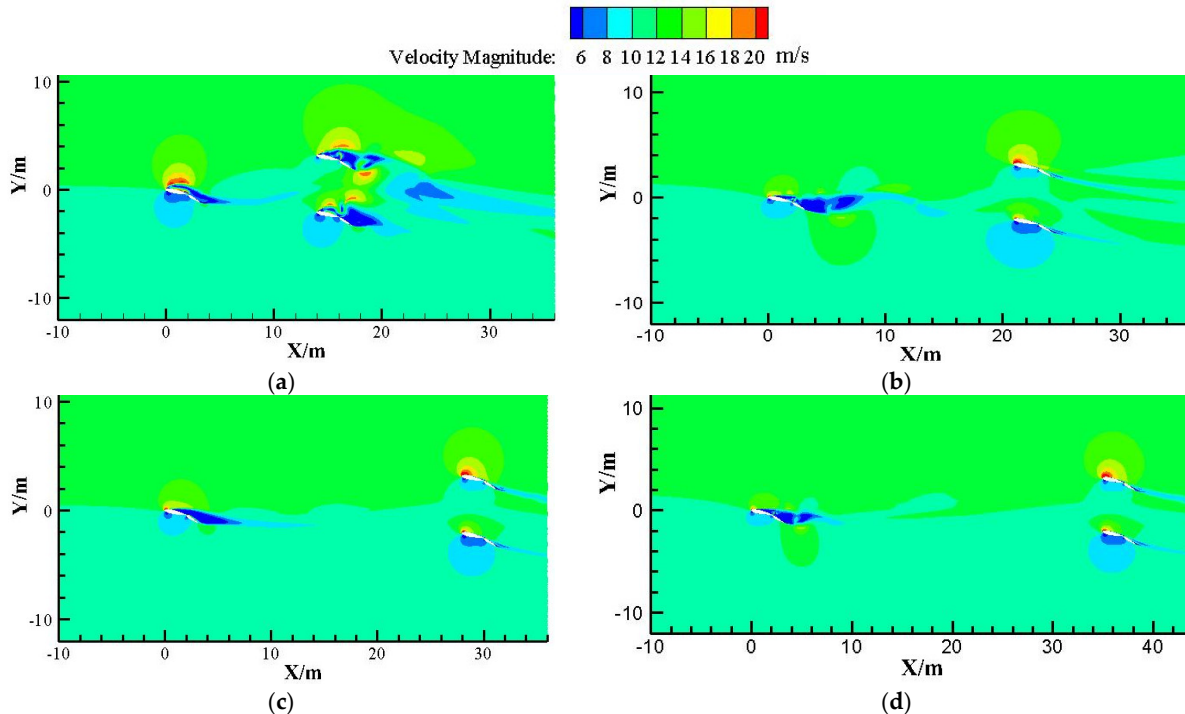


Figure 17. Layout of double-row two-element wingsail on deck.

Table 6. Layout scheme of double-row two-element wingsails on ship.

Types	Lateral Spacing	Structure 1	Structure 2	Structure 3	Structure 4
Longitudinal spacing	1.5c	4c	6c	8c	10c
	3c	4c	6c	8c	10c
	4c	4c	6c	8c	10c

**Figure 18.** Velocity distribution of two-element wingsails with different longitudinal spacings when the lateral spacing is 1.5c with the wind at $\theta = 90^\circ$. (a) Structure 1-1.5c. (b) Structure 2-1.5c. (c) Structure 3-1.5c. (d) Structure 4-1.5c.

In Figure 18, it can be seen that the low-speed range of Wingsail b1 and Wingsail b2 in the downstream wake of Structure 1-1.5c is large, with obvious flow separation. In addition, the wake of Wingsail a1 upstream is also separated by the interference of the downstream wingsail. Due to the increase in longitudinal spacing in Structure 2-1.5c, the low-speed wake region of Wingsail b1 and Wingsail b2 is significantly reduced. However, the wake of Wingsail a1 is still separated by the interference of downstream sails. The flow velocity distribution of Wingsail b1 and Wingsail b2 of Structure 3-1.5c and Structure 4-1.5c is relatively stable, and the low-speed wake area of the Wingsail a1 is significantly reduced. However, due to the small lateral spacing of the downstream sails, there is still a large flow separation, and it is necessary to increase the horizontal spacing of the downstream sails.

Subsequently, the streamlined distribution of Structure 3 and Structure 4 with lateral spacings of 3c and 4c was analyzed, as shown in Figure 19. In Figure 19a,b, it can be observed that there is still flow separation on the suction surface of the Wingsail a1 when the horizontal spacing is 3c. But its separation strength gradually decreases with the increase in the longitudinal spacing, and the interference effect of the downstream wingsail on the upstream wingsail wake is weakened. On this basis, the horizontal spacing was increased to 4c, as shown in Figure 19c. The suction surface separation of the Wingsail a1 weakens until the flow separation of all sails disappears, as shown in Figure 19d. To verify this result, the propulsion performances of each wingsail in Figure 19 were compared and analyzed, as shown in Table 6. In Table 7, it can be seen that the propulsion performance of Structure 4-4c is the best among the above schemes, with a 14.16% increase in the auxiliary

thrust coefficient compared to Structure 3-4c, while the side thrust coefficient is closest to zero, which meets the design requirements.

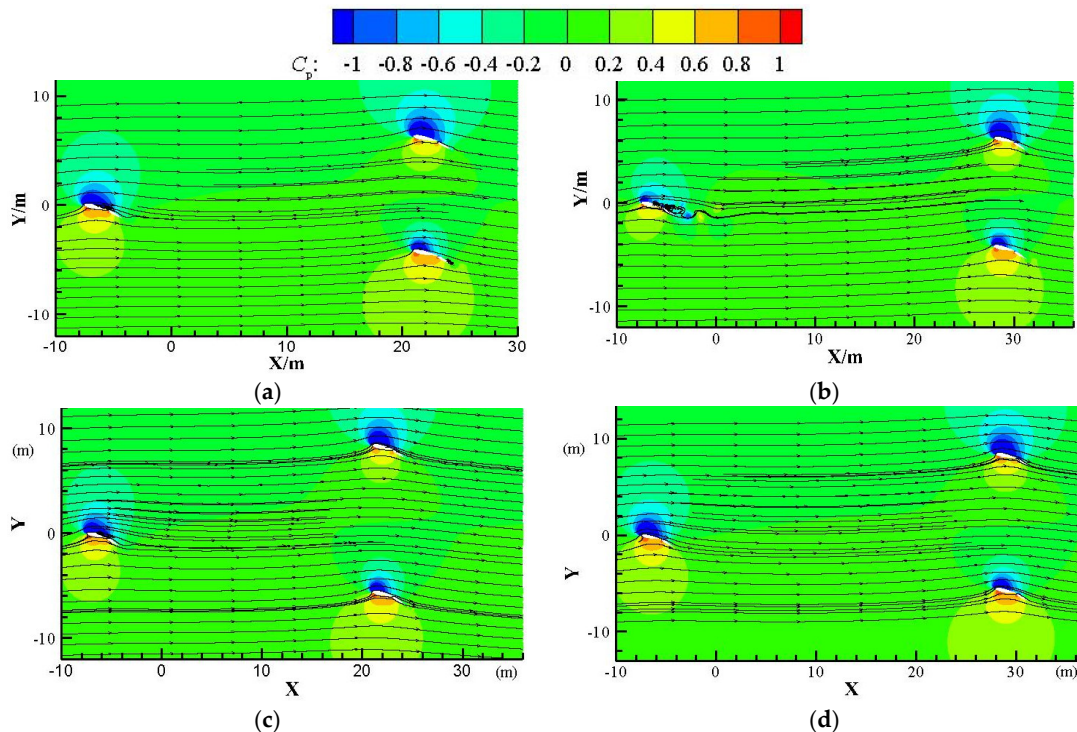


Figure 19. Streamlines of Structure 3 and Structure 4 when the lateral spacing is $3c$ and $4c$. **(a)** Structure 3-3c. **(b)** Structure 4-3c. **(c)** Structure 3-4c. **(d)** Structure 4-4c.

Table 7. Propulsion performance of the wingsails at different distances with the wind at $\theta = 90^\circ$.

Types	—	C_L	C_D	C_X	C_Y
Case 3-3c	Average value	2.080	0.107	2.076	0.107
Case 4-3c	Average value	1.870	0.112	1.871	0.112
Case 3-4c	Average value	2.098	0.108	2.098	0.108
Case 4-4c	Average value	2.444	0.063	2.444	0.063

3.5. Interference Characteristics of Double-Row Wingsails at a Relative Wind Direction Angle of 120°

By analyzing the flow field at a wind direction angle of 90° , it can be shown that the staggered arrangement of upstream and downstream sails can improve the impact of the upstream sail wake on downstream sails. For this reason, a staggered scheme with Case 4-4c was set up for the two-element wingsails with a wind direction angle of 120° , as shown in Table 8.

Table 8. Offset layout scheme of downstream wingsails.

Offset Layout Scheme for Downstream Wingsails	Scheme A	Scheme B	Scheme C	Scheme D
Lateral distance from Wingsail b1 to Wingsail a1	1.6c	2c	2.4c	2.8c

The impact of four different staggered arrangements on the aerodynamic performance of wingsails was analyzed, as shown in Figure 20. From Figure 20, it can be seen that, as the horizontal staggered distance between Wingsail b1 and Wingsail a1 increased, the overall auxiliary thrust coefficient of the wingsails first increased and then decreased, while the

side thrust first decreased and then increased. The auxiliary thrust coefficient of Scheme C was the highest at 2.444. Wingsail a1 in Scheme C had a significant increase of 22.34% compared to that in Scheme A.

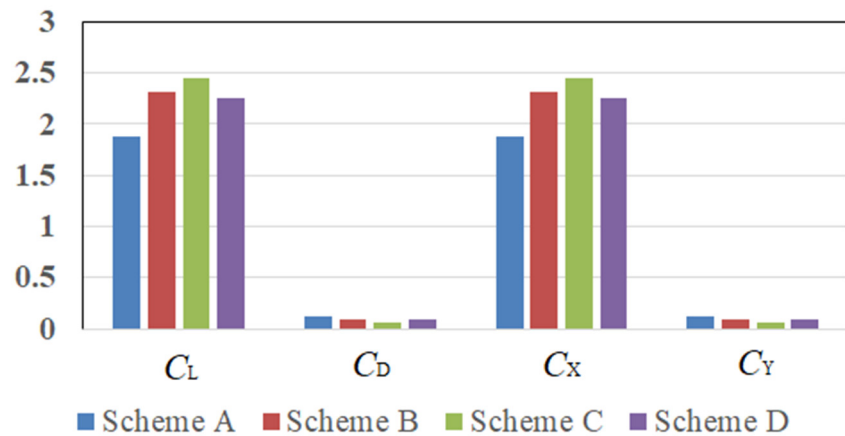


Figure 20. Performance comparison of the wingsails at different offset spacings with the wind at $\theta = 120^\circ$.

Figure 21 shows a velocity cloud map of the two-element wingsails of Scheme C with a wind direction angle of 120° . It can be seen from Figure 21 that the interference effect of the downstream wingsail on the upstream wingsail wake is weakened, and there is no flow separation phenomenon in the Wingsail b1. Therefore, the propulsion performance of the entire wingsail system is relatively high.

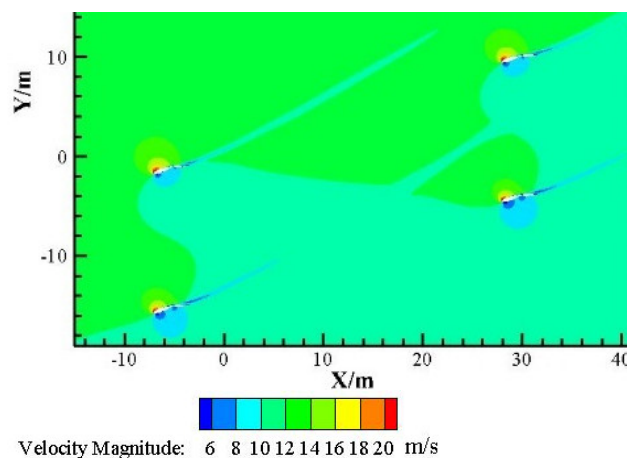


Figure 21. Velocity fields of two-element wingsails with Scheme C at $\theta = 120^\circ$.

4. Conclusions

The Reynolds averaged N-S equation was employed in the numerical simulation to analyze the performance of multiple sets of two-element wingsails under steady operating conditions. The inter-stage interference characteristics of the wingsails were obtained from the simulation.

The numerical calculation results indicate that, in the single-row arrangement scheme, a minimum horizontal spacing of $1.5c$ is optimal at relative wind angles of 30° , 90° , and 120° . At relative wind angles of 90° and 120° , inter-stage interference can cause wingsail stall and downstream wingsail flow separation. However, the optimal horizontal spacing for other relative wind directions is currently uncertain.

In the double-row arrangement schemes, the wake of the upstream wingsail interferes with the flow of the downstream sail at relative wind angles of 90° . And the propulsion

performance with a horizontal spacing of $4c$ and a longitudinal spacing of $10c$ is optimal. At the same time, the interference performance of the two-element wingsails can be further improved through a horizontal offset arrangement, at wind angles of 120° .

However, this study only considers a few representative relative wind direction angles, and the selected range of horizontal and vertical spacings is insufficient. In the future, we hope to conduct experimental research on the influence of wingsail interference characteristics.

Author Contributions: Conceptualization, C.L. and H.W.; investigation, C.L. and H.W.; methodology, C.L. and C.Z.; software, C.L. and J.Y.; writing—original draft preparation, C.L. and B.W.; writing—review and editing, H.W., C.Z. and B.W.; supervision, H.W. All authors have read and agreed to the published version of the manuscript.

Funding: This research was funded by the General Project of Natural Science Research in Jiangsu Universities, 20KJB580008.

Data Availability Statement: The data presented in this study are available on request from the corresponding author. The data are not publicly available due to the limitations of the study phase.

Conflicts of Interest: The authors declare no conflicts of interest.

References

1. Harilaos N., P. Market-based measures for greenhouse gas emissions from ships: A review. *WMU J. Marit. Aff.* **2012**, *11*, 211–232.
2. Marine Environment Protection Committee. *Initial IMO Strategy on Reduction of GHG Emissions from Ships*; IMO: London, UK, 2018.
3. Linda, S.; Hulda, W.; John, B. Greenhouse gas emissions from ships in ports—Case studies in four continents. *Transp. Res. Part D* **2017**, *54*, 212–224.
4. AYRO Raises €10.5M to Boost Development of Wingsail Technology. Available online: <https://cyprusshippingnews.com/2021/09/23/ayro-raises-e10-5-million-capital-to-boost-the-development-of-its-innovating-wingsail-solution-to-help-decarbonise-the-maritime-transport-industry/> (accessed on 17 September 2021).
5. Ross, J.C. Aerodynamic Design of a Rigid-Wing Sail for a C-Class Catamaran, The Ancient Interface XVIII. In Proceedings of the Eighteenth AIAA Symposium on the Aer/Hydronautics of Sailing; AIAA Lecture Series. AIAA Stanford: Stanford, CA, USA, 1989; Volume 35, pp. 17–27.
6. Elkaim, G.H. System Identification for Precision Control of a Wingsailed GPS-Guided Catamaran. Ph.D. Thesis, Stanford University, Stanford, CA, USA, 2001.
7. Elkaim, G.H.; Boycejrc, L. Experimental validation of GPS-based control of an unmanned wing-sailed catamaran. In Proceedings of the ION Global Navigation Satellite Systems Conference, Fort Worth, TX, USA, 25–28 September 2007; ION GNSS: Manassas, WV, USA, 2007; pp. 1950–1956.
8. Patrick, F.R.; Karl, D. Development and Preliminary Experimental Validation of a Wind- and Solar-Powered Autonomous Surface Vehicle. *IEEE J. Oceanic Eng.* **2010**, *35*, 971–982.
9. Cabrera-Gámez, J.; Ramos-de Miguel, A.; Domínguez-Brito, A.C.; Hernández-Sosa, J.D.; Isern-González, J.; Adler, L. A real-time sailboat controller based on chibios. In Proceedings of the 7th International Robotic Sailing Conference, Galway, Ireland, 9–12 September 2014; Robotic Sailing. Springer: Berlin/Heidelberg, Germany, 2014; pp. 77–85. [[CrossRef](#)]
10. Ocean Aero. Submaran™ S10: Wind and Solar-Powered Freedom to Go Further and Faster. Available online: <http://www.oceanaea.us/Ocean-Aero-Submaran> (accessed on 22 October 2017).
11. Saildrone. Saildrone 2016. Available online: <http://saildrone.com/#Technology> (accessed on 29 September 2017).
12. Autonomous Marine Systems. Available online: <http://www.automarinesys.com/> (accessed on 3 January 2018).
13. Dominguez-Brito, A.C.; Valle-Fernandez, B.; Cabrera-Gámez, J.; Ramos-de-Miguel, A. A-TIRMA G2: An oceanic autonomous sailboat. In *Robotic Sailing 2015*; Springer: Cham, Switzerland, 2016; pp. 3–13.
14. Fujiwara, T.; Hearn, G.E.; Kitamura, F.; Ueno, M. Sail-sail and sail-hull interaction effects of hybrid-sail assisted bulk carrier. *J. Mar. Sci. Technol.* **2005**, *10*, 82–95. [[CrossRef](#)]
15. Fujiwara, T.; Hearn, G.E.; Kitamura, F.; Ueno, M.; Minami, Y. Steady sailing performance of a hybrid-sail assisted bulk carrier. *J. Mar. Sci. Technol.* **2005**, *10*, 131–146. [[CrossRef](#)]
16. Jo, Y.; Choi, S.; Lee, H. Aerodynamic Design Optimization of Wingsails. In Proceedings of the 31st AIAA Applied Aerodynamics Conference, San Diego, CA, USA, 24–27 June 2013; p. 2524.
17. Li, Q.; Niheia, Y.; Nakashima, T.; Ikeda, Y. A study on the performance of cascade hard sails and sail-equipped vessels. *Ocean. Eng.* **2015**, *98*, 23–31. [[CrossRef](#)]
18. Zhang, T.; Zhang, J.; Yang, C. A data replenishment method for self regulating sail-assisted ships considering big data. In Proceedings of the Fifth International Conference on Advanced Cloud and Big Data (CBD), Shanghai, China, 13–16 August 2017; IEEE: Piscataway, NJ, USA, 2017.
19. Daniel, W.A. The CFD Assisted Design and Experimental Testing of a Wingsail with High Lift Devices. Ph.D. Thesis, University of Salford, Salford, UK, 1996.

20. Anderson, M.R. Aerodynamic Performance of a Small-Scale Wingsail Vessel. In Proceedings of the 54th AIAA Aerospace Sciences Meeting, San Diego, CA, USA, 4–8 January 2016.
21. Gao, H.; Zhu, W.; Liu, Y.; Yan, Y. Effect of various winglets on the performance of marine propeller. *Appl. Ocean Res.* **2019**, *86*, 246–256. [[CrossRef](#)]
22. Menter, F.R.; Langtry, R.B.; Likki, S.R.; Suzen, Y.B.; Huang, P.G.; Völker, S. A correlation-based transition model using local variables—Part I: Model formulation. *J. Turbomach.* **2006**, *128*, 413–422. [[CrossRef](#)]
23. Langtry, R.B.; Menter, F.R. correlation-based transition modeling for unstructured parallelized computational fluid dynamics codes. *AIAA J.* **2009**, *47*, 2894–2906. [[CrossRef](#)]
24. Celik, I.B.; Ghia, U.; Roache, P.J.; Freitas, C.J. Procedure for estimation and reporting of uncertainty due to discretization in CFD applications. *J. Fluids Eng.* **2008**, *130*, 078001.
25. Eça, L.; Hoekstrab, M. A procedure for the estimation of the numerical uncertainty of CFD calculations based on grid refinement studies. *J. Comput. Phys.* **2014**, *262*, 104–130. [[CrossRef](#)]
26. Timmer, W.A. Two-dimensional low-Reynolds number wind tunnel results for airfoil NACA 0018. *Wind. Eng.* **2008**, *32*, 525–537. [[CrossRef](#)]
27. Jacobs, E.N.; Sherman, A. Airfoil Section Characteristics as Affected by Variations of the Reynolds Number. *NACA Tech. Rep.* **1937**, *586*, 227–267.
28. Sheldahl, R.E.; Klimas, P.C. *Aerodynamic Characteristics of Seven Symmetrical Airfoil Sections through 180-Degree Angle of Attack for Use in Aerodynamic Analysis of Vertical Axis Wind Turbines*; Sandia National Laboratories: Albuquerque, NM, USA, 1981; SAND80-2114.
29. Gerakopoulos, R.; Boutilier, M.; Yarusevych, S. Aerodynamic Characterization of a NACA 0018 Airfoil at Low Reynolds Numbers. In Proceedings of the 40th Fluid Dynamics Conference and Exhibit, Chicago, IL, USA, 28 June–1 July 2010.
30. Raghunathan, S.; Ombaka, O.O. A thick symmetrical aerofoil oscillating about zero incidence angle. *Int. J. Heat Fluid Flow* **1986**, *7*, 155–159. [[CrossRef](#)]
31. Gao, H.; Zhu, W. Numerical investigation of bionic rudder with leading-edge protuberances. *J. Offshore Mech. Arct. Eng.* **2020**, *142*, 011802. [[CrossRef](#)]

Disclaimer/Publisher's Note: The statements, opinions and data contained in all publications are solely those of the individual author(s) and contributor(s) and not of MDPI and/or the editor(s). MDPI and/or the editor(s) disclaim responsibility for any injury to people or property resulting from any ideas, methods, instructions or products referred to in the content.